



# Magnetic Recyclable Double-Heterojunction SrFe<sub>12</sub>O<sub>19</sub>/SnS<sub>2</sub>/MoS<sub>2</sub> Nanophotocatalyst: Synthesis and Visible-Light Catalytic Degradation Performance Study

Bi Jia<sup>1</sup> · Qian Cai<sup>2</sup> · Yongjiang Di<sup>1</sup> · Huichao He<sup>1</sup> · Tao Han<sup>1</sup> · Hanmei Jiang<sup>1</sup> · Shiyu Lu<sup>1</sup> · Rong Wang<sup>1</sup> · Yue Shi<sup>1</sup>

Received: 1 March 2024 / Revised: 3 June 2024 / Accepted: 4 June 2024 / Published online: 7 June 2024  
© The Author(s), under exclusive licence to Korean Institute of Chemical Engineers, Seoul, Korea 2024

## Abstract

The development of efficient, recyclable, broad-spectrum photocatalysts was the primary objective in the field of photocatalytic wastewater degradation. Herein, a novel highly efficient ternary magnetic semiconductor composite was synthesized by integrating SrFe<sub>12</sub>O<sub>19</sub>, MoS<sub>2</sub> nanoflower clusters, and SnS<sub>2</sub> nanoflowers using high-temperature calcination and a one-step solvothermal method. The synthesized heterojunction nanocomposite was characterized using numerous analytical techniques, and its photocatalytic activity was evaluated under half sunlight intensity irradiation. The integration of SnS<sub>2</sub> with SrFe<sub>12</sub>O<sub>19</sub> and MoS<sub>2</sub> effectively modified the crystal structure and morphology of SnS<sub>2</sub> nanoflowers, leading to an increase in active sites while overcoming the significant electron–hole recombination rates of the individual components. The SrFe<sub>12</sub>O<sub>19</sub>/SnS<sub>2</sub>/MoS<sub>2</sub> composite achieved 98.69% degradation of MB dye at a suitable pH of 6 and a period of 120 min of irradiation. Additionally, it maintained an excellent magnetic phenomena which contributed to it effortless to collect and reclaim from the residual mixture. After three cycles, the MB dye degradation remained at 84.07%, demonstrating its endurance and resilience. The scavenger test identified the superoxide radical as the primary agent responsible for dye destruction. This work provides study presents a synthesis method for highly efficient photocatalysts using in natural visible-light that can be recovered by simply applying an external magnetic field.

**Keywords** Photocatalysis · Nanostructures · Heterojunctions · Visible-light degradation · Magnetic recovery

## Introduction

With the development of science and technology, economy and industry, a vast array of chemical manufacturing goods have become a part of people's daily lives [1–3]. While these goods deliver multiple conveniences, but are also synonymous with adverse environmental impacts and wasteful use of energy. Organic dye-containing effluent from the textile industry is released in substantial amounts into rivers and

groundwater; such contaminants are hazardous and slow to break down [4]. Fujishima and Honda pioneered the use of photocatalysis to address environmental pollution in 1972 by employing TiO<sub>2</sub> to catalytically decompose water into H<sub>2</sub> and O<sub>2</sub> under UV-light irradiation [5]. This delivers an alternative viewpoint on the treatment of sewage. Photocatalysis is a promising emerging technology that may advance the fields of new energy and environmental protection by using solar energy to degrade pollutants in water [6]. Accordingly, the performance of photocatalysts is a critical component of this technology. Thus, the development of effective, environmentally sustainable, visible-light-responsive photocatalysts has emerged as a fresh field of interest for investigation [7].

Currently, researchers are focusing on combined semiconductors and tiny particles in which quantization properties have been approximated, along with semiconductors on passive supports [8]. Photocatalytic semiconductor materials with controlled morphologies have produced numerous favorable results in environmental remediation processes [9, 10]. Metal sulfides are of particular interest owing to

✉ Yongjiang Di  
yjdee@cqust.edu.cn

✉ Yue Shi  
pache927@163.com

<sup>1</sup> School of Metallurgy and Materials Engineering, Chongqing University of Science and Technology, Chongqing 401331, China

<sup>2</sup> School of Chemistry and Chemical Engineering, Chongqing University of Science and Technology, Chongqing 401331, China

their narrow band gap (approximately 1.8 eV), high solar energy utilization, and excellent carrier mobility, which allow them to meet the demanding thermodynamic requirements of reactions including the decomposition of aquatic hydrogen [11, 12], CO<sub>2</sub> reduction [13, 14], and degradation of organic pollutants [15]. SnS<sub>2</sub>, a representative sulfide, is a visible-light photocatalyst with significant development potential owing to its relatively small band gap (2.1 eV), laminar framework, vast relative area of surface, multiple sites of action, superior chemical rigidity, non-toxic nature, and a relatively inexpensive price [16–18]. For instance, Liu et al. prepared SnS<sub>2</sub> nanosheets with major (0 0 1) facets by liquid-phase stripping. When compared with bulk SnS<sub>2</sub>, SnS<sub>2</sub> nanosheets exhibit superior photocatalytic capacity due to their significantly effective charge separation [18]. Wang et al. synthesized SnS<sub>2</sub> via the melting process, which features a flower-like hierarchical structure formed by nano-flake assembly. The SnS<sub>2</sub> nanoflowers synthesized by low-temperature melting approach illustrated superior photocatalytic abilities than the SnS<sub>2</sub> nanoplates manufactured by hydrothermal method [19]. Tragically, the photocatalytic capabilities of SnS<sub>2</sub> composites is limited by the rapid recombination of photogenerated electrons and holes both on the exterior and inside the material's bulk [20, 21]. Therefore, it is required to develop effective methods to further ameliorate the photocatalysis activity.

In recent years, constructing heterojunction-modified semiconductor photocatalytic materials has been one of the most effective strategies to ameliorate the photocatalytic activity of a single semiconductor, because of their enhanced light absorption ability as well as accelerated charge carrier transfer and separation [22]. Up-to-date, several attempts have been made to alter the electron band structure, laminar framework, and charge separation capacity of metal sulfides to boost the activity of photocatalytic decomposition. The photogenerated charge separation in SnS<sub>2</sub> layered materials can be improved by forming heterojunctions with other semiconductor photocatalysts (such as g-C<sub>3</sub>N<sub>4</sub> [17], ZnS [23], Bi<sub>2</sub>S<sub>3</sub> [24], SnO<sub>2</sub> [25], and MgFe<sub>2</sub>O<sub>4</sub> [16]). As a two-dimensional transition-metal disulfide and narrow-band-gap semiconductor, MoS<sub>2</sub> has garnered significant attention owing to its high carrier mobility, exceptional photostability, expansive specific surface area, distinctive photoelectrochemical properties, and adjustable band gap energy (1.2–1.9 eV) [26]. MoS<sub>2</sub> has been widely utilized in a wide range of applications, including photocatalysis [4, 27–29], sensors [30–32], dye-sensitized batteries [33–35], and lithium-ion batteries [36, 37]. Moreover, the band structure of MoS<sub>2</sub> can well match that of SnS<sub>2</sub>, and therefore, a SnS<sub>2</sub>/MoS<sub>2</sub> heterojunction was synthesized to promote the photocatalytic activity of SnS<sub>2</sub>. While coupling SnS<sub>2</sub> to MoS<sub>2</sub> alone has made strides in addressing some of the issues related to their photoresponsivity, these materials still struggle to achieve

efficient recycling or rapid charge carrier separation. The separation of these photocatalysts from a mixture following a photocatalyst reaction remains a challenge, limiting their applications [38]. Ferrite can quickly and efficiently recycle photocatalysts; thus, hard magnetic ferrites have attracted considerable attention for magneto-optical applications owing to their high magnetic energy products, high saturation magnetization strength and coercivity, and strong thermal stability [39, 40]. SrFe<sub>12</sub>O<sub>19</sub> exhibits characteristics, such as corrosion resistance, high mechanical stability, and cost-effectiveness [41]. It is encouraging to observe that adding a third semiconductor SrFe<sub>12</sub>O<sub>19</sub> enables rapid separation from the mixture and significantly boosts the photocatalytic efficiency by improving redox capacity and electron–hole pair mobility. The literature indicates that there is an appropriate match between the energy band structure of SrFe<sub>12</sub>O<sub>19</sub> and MoS<sub>2</sub> [42]. Hence, it is anticipated that adding SrFe<sub>12</sub>O<sub>19</sub> into SnS<sub>2</sub>/MoS<sub>2</sub> will substantially decrease electron–hole complexation as well as improve photocatalytic capacity. These photocatalysts can be easily separated and recovered using a magnetic field [43].

In this study, a novel, highly efficient ternary SrFe<sub>12</sub>O<sub>19</sub>/SnS<sub>2</sub>/MoS<sub>2</sub> magnetic semiconductor composite photocatalyst with double-heterojunction was synthesized by growing SrFe<sub>12</sub>O<sub>19</sub> particles and MoS<sub>2</sub> nanoflower clusters on SnS<sub>2</sub> nanoflower carriers using high-temperature calcination and a one-step solvothermal method. Furthermore, the influence of the SrFe<sub>12</sub>O<sub>19</sub> content and dye pH on the photocatalytic performance and the mechanism by which the ternary heterojunction with a unique flower-like morphology formed on the surface were evaluated.

## Materials and Methods

Strontium chloride hexahydrate (SrCl<sub>2</sub>·6H<sub>2</sub>O), ferric chloride hexahydrate (FeCl<sub>3</sub>·6H<sub>2</sub>O), sodium molybdate dihydrate (Na<sub>2</sub>MoO<sub>4</sub>·2H<sub>2</sub>O), tin tetrachloride pentahydrate (SnCl<sub>4</sub>·5H<sub>2</sub>O), thiourea (CH<sub>4</sub>N<sub>2</sub>S), sodium hydroxide (NaOH), anhydrous ethanol (C<sub>2</sub>H<sub>5</sub>OH), isopropanol (C<sub>3</sub>H<sub>8</sub>O), and concentrated nitric acid (HNO<sub>3</sub>) were purchased from Chengdu Kolon Chemical Co., China. P-benzoquinone (C<sub>6</sub>H<sub>4</sub>O<sub>2</sub>) and disodium ethylenediaminetetraacetic acid (C<sub>10</sub>H<sub>14</sub>N<sub>2</sub>Na<sub>2</sub>O<sub>8</sub>·2H<sub>2</sub>O) were purchased from Shanghai McLean Biochemical Technology Co., China. All reagents were analytically pure and did not need any extra purification. Ultrapure water was used in all procedures.

The crystal phase compositions of the samples were determined by X-ray diffraction (SmartLab-9, Rigaku, Japan) using a Cu K $\alpha$  ( $\lambda = 0.154$  nm) radiation source over a  $2\theta$  scanning range of 10°–80° at a scanning speed of 0.05°s<sup>-1</sup>. The morphology and energy-dispersive spectra (EDS) of the samples were tested and characterized

by a field-emission scanning electron microscope (FE-SEM, JSM-7800F, Nippon Electronics JEOL, Japan). The microstructure and lattice fringe of the samples were examined by high-resolution transmission electron microscopy (HRTEM, JE-2100F, Nippon Electronics JEOL, Japan). X-ray photoelectron spectroscopy (XPS, Thermo Scientific K-Alpha, USA) was used to analyze the elemental valences and chemical composition of the composite photocatalyst. The specific surface areas of the samples obtained through N<sub>2</sub> adsorption apparatus (ASAP 2460, Micromeritics, USA). Ultraviolet–visible (UV–Vis) diffuse reflectance spectra (DRS) absorption spectra was performed using a spectrophotometer (Beijing Puxi General Instrument Co., Ltd., China) with a BaSO<sub>4</sub> reference material. The photoluminescence (PL) spectrum spanning 350–800 nm was obtained with a fluorescence spectrometer (FLS1000, Edinburgh Instruments Ltd., UK). The magnetic properties of the samples were characterized using an MPMS3 magnetic test system (Quantum Company, USA). Electrochemical impedance spectroscopy (EIS) was performed using a PGSTAT302N comprehensive electrochemical workstation (Metrohm Corp., Switzerland).

### Synthesis of SrFe<sub>12</sub>O<sub>19</sub> Hexagonal Single Crystal Particles

SrFe<sub>12</sub>O<sub>19</sub> was prepared by an established wet chemical method [42].

### Synthesis of Magnetic Composite SrFe<sub>12</sub>O<sub>19</sub>/SnS<sub>2</sub>/MoS<sub>2</sub>

One-step solvothermal synthesis was utilized to generate magnetic materials [23]. Na<sub>2</sub>MoO<sub>4</sub>·2H<sub>2</sub>O (1 mmol), SnCl<sub>4</sub>·5H<sub>2</sub>O (1 mmol), and thiourea (4 mmol) were dissolved in ultrapure water (10 mL) by ultrasonication for 30 min, following which isopropanol (40 mL) was added and the combination was mechanically swirled approximately 20 min to ensure an even distribution. SrFe<sub>12</sub>O<sub>19</sub> with molar ratios to SnS<sub>2</sub> with 1:16, 1:8, 1:4, and 1:2 was dissolved in the mixture and dispersed throughout 1 h of mechanical and ultrasound agitation. After that, the mixture was inserted to a high-pressure reaction kettle and allowed to sit for 22 h at 200 °C. Following the reaction, the solution was chilled to 20 °C and separated. After being washed with water and ethanol four times, the samples had been filtered and dehydrated for 12 h at 80 °C. The composites synthesized with SrFe<sub>12</sub>O<sub>19</sub>, SnS<sub>2</sub>, and MoS<sub>2</sub> in mass ratios of 1:16:16, 1:8:8, 1:4:4, and 1:2:2 were labeled SSM-I, SSM-II, SSM-III, and SSM-IV, respectively. Similar steps were utilized to synthesize pristine SnS<sub>2</sub> and MoS<sub>2</sub>, omitting the preliminary addition of SrFe<sub>12</sub>O<sub>19</sub>. A schematic of the synthesis of the magnetic composites is shown in Fig. 1.

### Photocatalytic Performance

The photocatalytic properties of the materials were evaluated by examining their ability to decompose methylene blue (MB) solutions in the absence of visible light. A catalyst sample

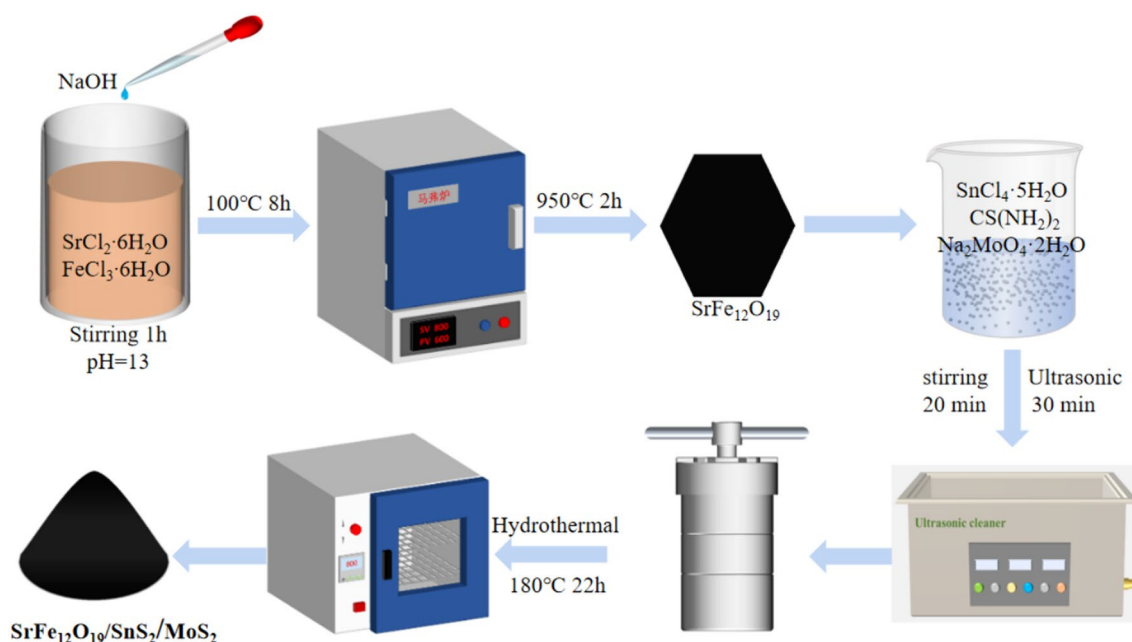


Fig. 1 Synthesis of the SrFe<sub>12</sub>O<sub>19</sub>/SnS<sub>2</sub>/MoS<sub>2</sub> composite photocatalyst

(30 mg) was dispersed in an MB solution (80 mL, 20 mg/L) and swirled in the dark approximately 30 min to accomplish an equilibrium of adsorption and desorption [44–46]. The reaction was then performed at 26 °C under simulate half sunlight intensity, which was close to the actual lighting in nature. After 20 min, an aliquot (5 mL) of the solution was centrifuged to determine the absorbance at 664 nm. To minimize the impact of volume reduction on subsequent catalysis, stirring was maintained during the photocatalytic degradation experiment to keep the catalyst uniformly dispersed. This ensured that the reduction of the catalyst was proportional to the solution volume when samples were collected. Equation (1) has been utilized to compute the MB degradation ratio [42]:

$$\eta = (A_0 - A_t) / A_0 \times 100\% \quad (1)$$

where  $\eta$  is the degradation ratio,  $A_0$  is the absorbance of the MB solution after achieving adsorption–desorption equilibrium, and  $A_t$  is the absorbance of the MB solution after illumination for time  $t$ . Further, the photocatalytic stability and recyclability of the SrFe<sub>12</sub>O<sub>19</sub>/SnS<sub>2</sub>/MoS<sub>2</sub> composite photocatalysts were evaluated using cyclic tests under the same conditions. The degradation efficiency of the SrFe<sub>12</sub>O<sub>19</sub>/SnS<sub>2</sub>/MoS<sub>2</sub> composite was examined over three consecutive cycles in the photodegradation of a 20 mg/L solution of MB at pH 6, with a catalyst loading of 375 mg/L. Following each photodegradation experiment, the photocatalysts were retrieved using an external magnet, cleansed with ethanol and distilled water, and subsequently dried in an oven at 60 °C.

### Active Radicals Capturing Research

The major active radicals trapping text was performed in the similar manner to the photocatalytic decomposition experiment, with the only difference being the inclusion of various scavengers [47]. A solution of BQ (1 mmol/L), a solution of EDTA-2Na (1 mmol), and a solution of IPA (1 mmol) were employed as scavengers for superoxide anion ( $\cdot\text{O}_2^-$ ), hydrogen peroxide ( $\text{H}_2\text{O}_2$ ), and hydroxyl radical ( $\cdot\text{OH}$ ), respectively.

## Results and Discussion

### Photocatalyst Characterization

The X-ray diffraction (XRD) patterns of SrFe<sub>12</sub>O<sub>19</sub>, SnS<sub>2</sub>, MoS<sub>2</sub>, and SSM composites with various compositions are presented in Fig. 2. Over the 2 $\theta$  range of 10°–80°, sharp and intense peaks corresponding to pure SrFe<sub>12</sub>O<sub>19</sub> (JCPDS:84–1531) are observed at 30.39°, 32.40°, 34.23°, 37.19°, 40.47°, 42.55°, 55.20°, 56.89°, and 63.15°. These peaks are attributed to the (1 1 0), (1 0 7), (1 1 4), (2 0

3), (2 0 5), (2 0 6), (2 1 7), (2 0 11), and (2 2 0) crystal planes [40, 42], in the order. The highest-intensity spikes at 14.98°, 28.19°, 32.12° and 49.96° correspond to the (0 0 1), (1 0 0), (1 0 1) and (1 1 0) crystal planes of pure SnS<sub>2</sub> (JCPDS:23–0677), respectively [18]. The characteristic spike at 34.19° is associated with the (0 1 2) crystal plane of MoS<sub>2</sub> (JCPDS:17–0744), which exists in an amorphous state with low crystallinity [22]. The diffraction peak of the (0 0 1) crystal plane of single-phase SnS<sub>2</sub> is enhanced by the solvothermal synthesis as a characteristic of its layered material properties [48]. This layered structure is also confirmed by the SEM morphology. The XRD spectrum of the SrFe<sub>12</sub>O<sub>19</sub>/SnS<sub>2</sub>/MoS<sub>2</sub> composite photocatalyst is similar to that of pure SrFe<sub>12</sub>O<sub>19</sub>, indicating that SrFe<sub>12</sub>O<sub>19</sub> is the dominant crystalline phase. The peaks at 28.19° and 52.45° still show the characteristic peaks of SnS<sub>2</sub>. However, in the presence of a magnetic field environment with SrFe<sub>12</sub>O<sub>19</sub> ferrite particles, the co-synthesis of SrFe<sub>12</sub>O<sub>19</sub> and MoS<sub>2</sub> via one-step solvothermal synthesis alter the chemical reaction environment, crystallization, and growth dynamics of SnS<sub>2</sub>, creating stress or defects that reduce or shift the intensity of the (0 0 1) diffraction peak [48–50]. Moreover, in the composite of SnS<sub>2</sub> with SrFe<sub>12</sub>O<sub>19</sub> and MoS<sub>2</sub>, the introduction of components such as Mo, Sr, Fe and O, also results in some doping or vacancies, significantly affecting the intensity of specific diffraction peaks, further reducing or shifting the (0 0 1) peak intensity [49, 50].

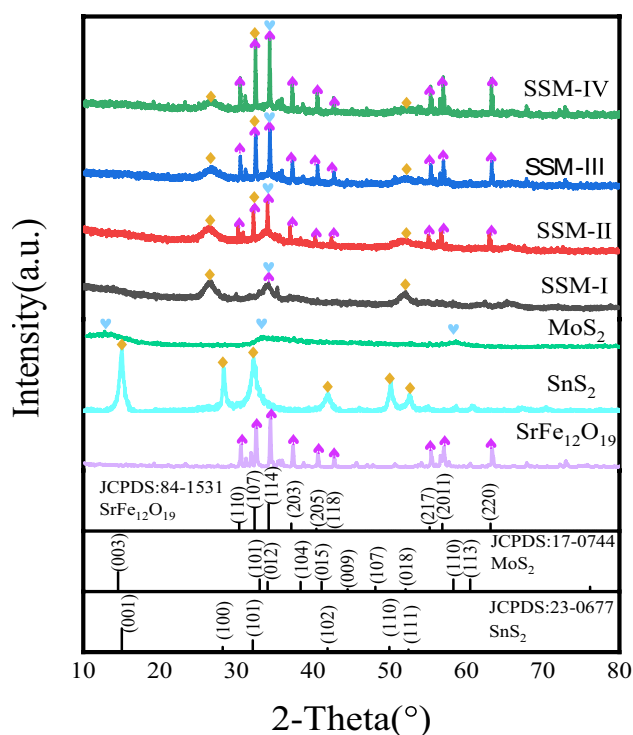


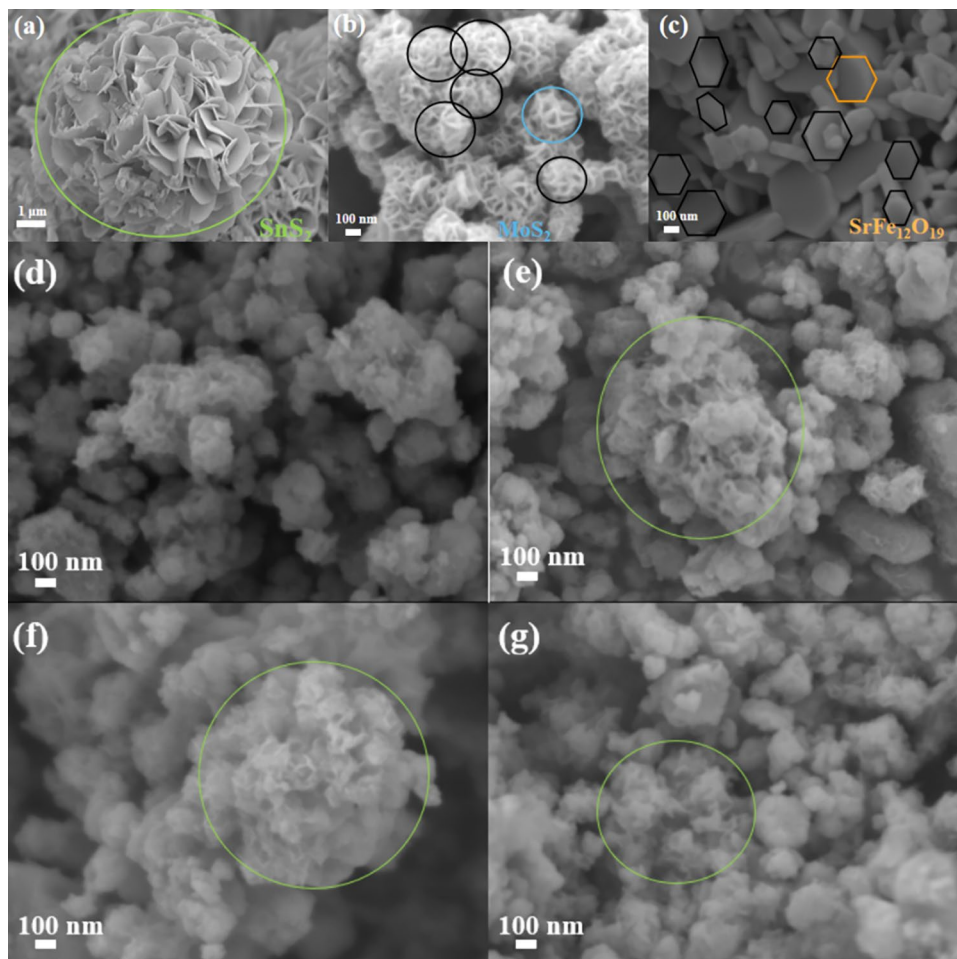
Fig. 2 XRD pattern of the composite catalysts and their components

The morphology of the photocatalysts and their constituents was characterized using FE-SEM. The 3D flower-like SnS<sub>2</sub> microspheres consist of randomly arranged 2D SnS<sub>2</sub> nanosheets (Fig. 3a). Hexagonal SrFe<sub>12</sub>O<sub>19</sub> (Fig. 3c) and cluster-like nanoflower MoS<sub>2</sub> (Fig. 3b), with an average diameter of approximately 200 nm, are properly distributed on the 3D SnS<sub>2</sub> microspheres. FE-SEM images of the composite catalysts are shown in Fig. 3d–g. Groups of SnS<sub>2</sub> blooms are wrapped around each other, while the SrFe<sub>12</sub>O<sub>19</sub> nanosheets and MoS<sub>2</sub> blooms uniformly penetrate the SnS<sub>2</sub> nanoflakes. This mixed structure increases the number of exposed interface regions between SrFe<sub>12</sub>O<sub>19</sub>, MoS<sub>2</sub>, and SnS<sub>2</sub>. Notably, the agglomeration of SrFe<sub>12</sub>O<sub>19</sub> nanoparticles in the composite increases with the SrFe<sub>12</sub>O<sub>19</sub> content (Fig. 3f, g), hindering their insertion into the SnS<sub>2</sub> nanosheets. The changes in the layered appearance of SSM in the SEM morphology and the most prominent (1 0 0) plane observed in the HRTEM confirm the structural changes of SnS<sub>2</sub> before and after compositing. These changes facilitate the exposure of the (1 0 0) plane of SnS<sub>2</sub>, increasing the active sites and accelerating the kinetics of electron and ion diffusion, thereby enhancing photocatalytic

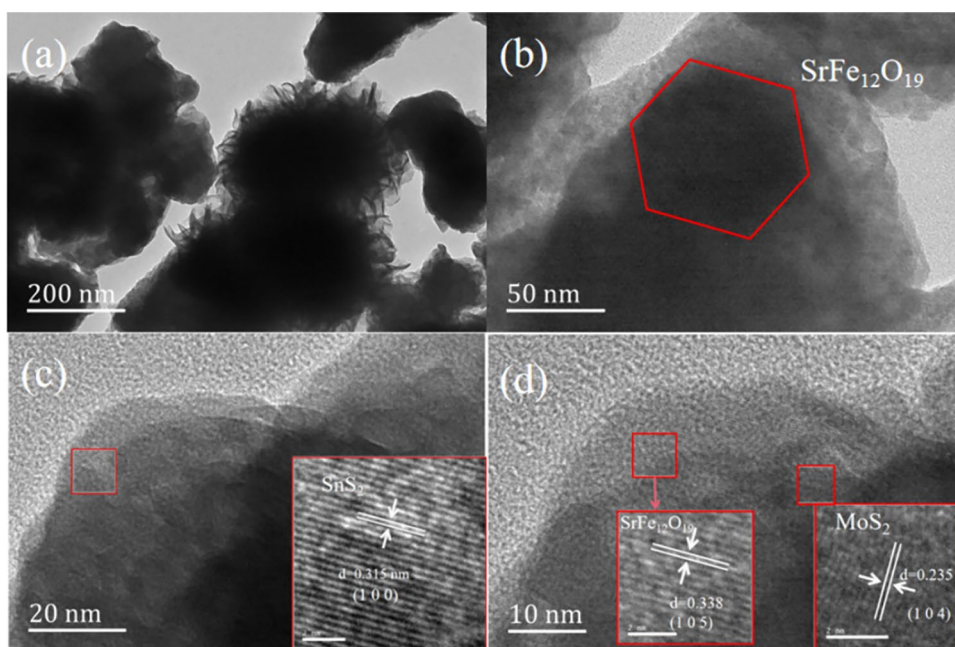
activity [51]. The strategy of altering and exposing diffraction peaks through compositing makes SnS<sub>2</sub> composites a promising candidate for efficient photocatalytic materials.

Figure 4 shows the HRTEM images of the internal structure of the SSM-II composite. The pristine SnS<sub>2</sub> and MoS<sub>2</sub> nanosheets are thin and the SnS<sub>2</sub> coating on the hexagonal SrFe<sub>12</sub>O<sub>19</sub> microcrystals indicates association between SrFe<sub>12</sub>O<sub>19</sub> and SnS<sub>2</sub> (Fig. 4a, b). The junction area between the three materials (Fig. 4c, d) exhibits individual crystalline regions of SrFe<sub>12</sub>O<sub>19</sub>, SnS<sub>2</sub>, and MoS<sub>2</sub>, signifying the synthesis of SSM mixtures. Streaks consisting of SrFe<sub>12</sub>O<sub>19</sub>, SnS<sub>2</sub>, and MoS<sub>2</sub> lattices are also shown. The lattice with an interlayer gap of 0.315 nm is linked with the SnS<sub>2</sub> (1 0 0) plane [16], while the lattices with interlayer gaps of 0.338 and 0.235 nm are linked with the SrFe<sub>12</sub>O<sub>19</sub> (1 0 5) and MoS<sub>2</sub> (1 0 4) crystal planes, respectively [22, 43]. EDS maps of the photocatalysts, presented in (Fig. 5), confirm the presence and uniform distribution of O, S, Fe, Sr, Mo, and Sn in the SSM-II. The synthesized SSM composite not only exhibits the crystal structures of SrFe<sub>12</sub>O<sub>19</sub>, SnS<sub>2</sub>, and MoS<sub>2</sub> but also benefits from the induced crystal structure defects and the

**Fig. 3** FE-SEM images of pure SnS<sub>2</sub> (a), MoS<sub>2</sub> (b), SrFe<sub>12</sub>O<sub>19</sub> (c), SSM-I (d), SSM-II (e), SSM-III (f), and SSM-IV nanoplate composite (g)



**Fig. 4** **a, b** TEM image of SSM-II; **c, d** HRTEM images of the  $\text{SnS}_2$ ,  $\text{SrFe}_{12}\text{O}_{19}$ , and  $\text{MoS}_2$  composites



exposure of crystal planes during the compositing process, which collectively enhance its photocatalytic activity.

### Physicochemical Properties

The XPS analysis of the magnetic composite photocatalyst SSM-II revealed the presence of Mo, Sn, O, S, Fe, and Sr (Fig. 6a). The binding energy of O 1s (530.99 eV, Fig. 6b) corresponds to the lattice oxygen in crystalline  $\text{SrFe}_{12}\text{O}_{19}$ . Sr 3d<sub>5/2</sub> and Sr 3d<sub>3/2</sub> are accountable for the peaks situated at 133.38 and 139.3 eV, respectively. According to a previous investigation, Sr 3d<sub>3/2</sub> explains the existence of Sr<sup>2+</sup> and Sr 3d<sub>5/2</sub> is generated from the chemical link Sr–O (Fig. 6c) [52]. The existence of ions containing Fe<sup>3+</sup> in strontium ferrite provides the reason for the binding energies of the Fe 2p<sub>3/2</sub> peaks (711.68 and 716.24 eV, Fig. 6d) [42]. The Sn 3d curves are extremely smooth and symmetrical (Fig. 6e). The Sn 3d<sub>5/2</sub> and Sn 3d<sub>3/2</sub> areas in  $\text{SnS}_2$  are represented by the peaks approximately 486.60 eV and 494.94 eV, respectively. The peaks at 228.8 and 231.9 eV in the Mo 3d spectrum correspond to Mo 3d<sub>5/2</sub> and Mo 3d<sub>3/2</sub>, respectively, demonstrating a 4+ Mo oxidative form. The generation of Mo<sup>6+</sup> by the moderate oxidation of  $\text{MoS}_2$  is to blame for the satellite peak (235.7 eV) [53]. A 2 S peak (226.24 eV) is also attributed to  $\text{MoS}_2$  (Fig. 6f). The XPS profile of S 2p (Fig. 6g) shows peaks at 161.53 and 162.83 eV that correspond to S 2p<sub>3/2</sub> and S 2p<sub>1/2</sub>, respectively, reflecting the spin orbit separation of S. An additional peak at 169.13 eV is attributed to polysulfide S<sup>2-</sup>.  $\text{SnS}_2$  and  $\text{MoS}_2$  were effectively incorporated into  $\text{SrFe}_{12}\text{O}_{19}$ , as indicated by the existence of S 2p and S<sup>2-</sup> [14].

### Nitrogen Adsorption

Other crucial factors affecting the performance of the photocatalytic material include the specific surface area and pore size of the catalyst. The N<sub>2</sub> adsorption–desorption isotherms of the  $\text{MoS}_2$ ,  $\text{SnS}_2$ ,  $\text{SrFe}_{12}\text{O}_{19}$ , and SSM-II samples are shown in Fig. 7. The N<sub>2</sub> adsorption–desorption results show a type IV isotherms with type H3 hysteresis loops, indicating that the material possesses a mesoporous characteristics [25]. The composite sample SSM-II exhibits the similar curve as does pure  $\text{SnS}_2$ , indicating that the composite retains the mesoporous characteristics of pure  $\text{SnS}_2$  [54]. Compared to SSM-II and  $\text{SnS}_2$ ,  $\text{SrFe}_{12}\text{O}_{19}$  and  $\text{MoS}_2$  exhibits a lower adsorption rate and does not show clear characteristics of type III or type IV adsorption isotherms, which is consistent with the specific surface area test results. The low adsorption rate of strontium ferrite is unfavorable for photocatalytic degradation, but its adsorption rate can be improved through composite formation. Table 1 lists the specific surface areas ( $S_{\text{BET}}$ ) and pore volumes of all materials.  $\text{SnS}_2$  possesses the largest specific surface area owing to its spherical nanoflower structure. The addition of  $\text{SrFe}_{12}\text{O}_{19}$  gradually destroyed the original flower-like spherical structure of  $\text{SnS}_2$ , reducing the specific surface area of the composite. However, the specific surface areas of the composites are significantly higher than those of  $\text{MoS}_2$  and  $\text{SrFe}_{12}\text{O}_{19}$ , subsequently reducing the probability of electron–hole recombination and improving the degradation efficiency.

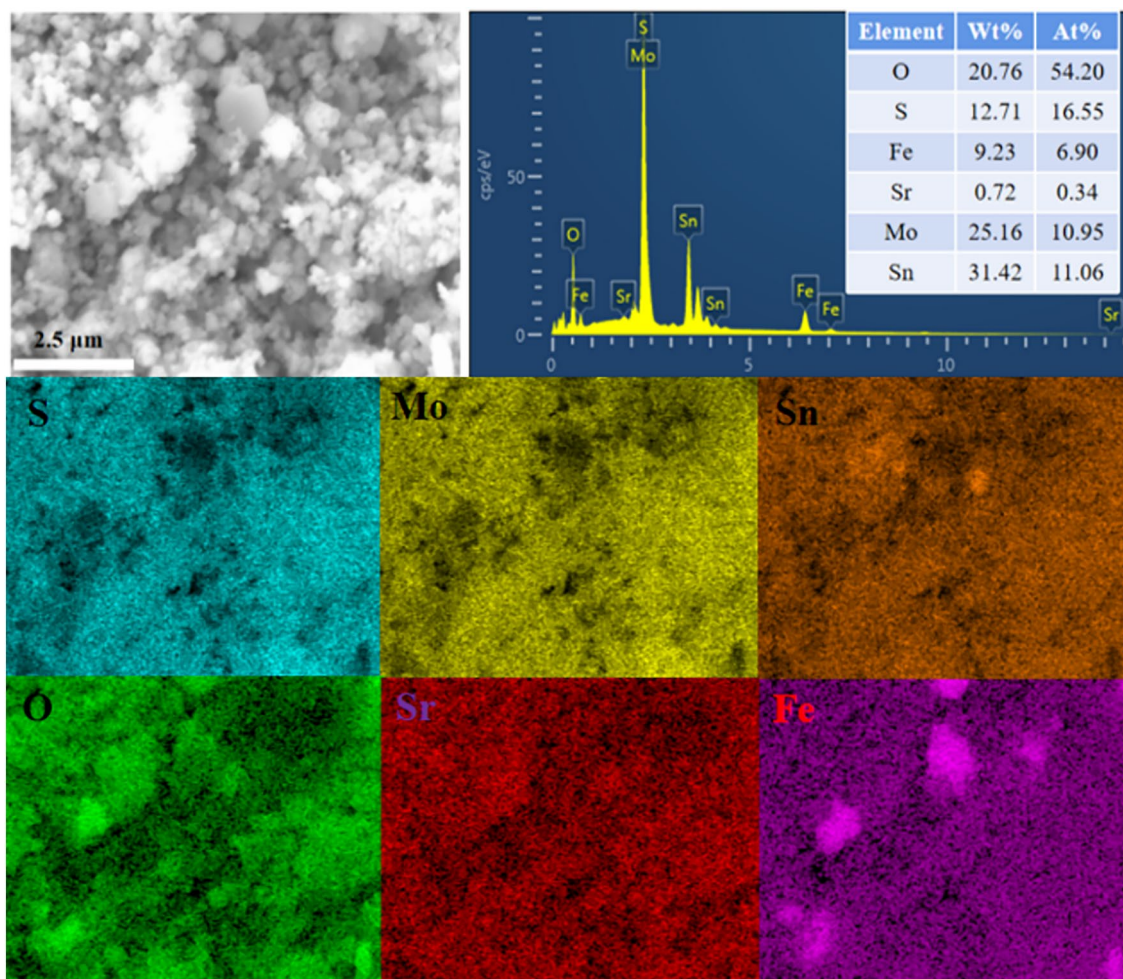


Fig. 5 EDS images and spectrum of SSM-II

### Electrochemical Impedance and Optical Property

Performance in photocatalysis depends on by the capacity of the composites to absorb light. Figure 8a shows the UV–vis absorption spectra of SrFe<sub>12</sub>O<sub>19</sub>, MoS<sub>2</sub>, SnS<sub>2</sub>, and SSM materials with various compositions. All the photocatalytic materials exhibit strong absorption over the full range of wavelengths. The SSM composites exhibit a higher UV–vis intensity than do pure SrFe<sub>12</sub>O<sub>19</sub>, SnS<sub>2</sub>, and MoS<sub>2</sub>, with SSM-II having the strongest absorbance. The forbidden bandwidth is estimated by Eq. (2) [55]:

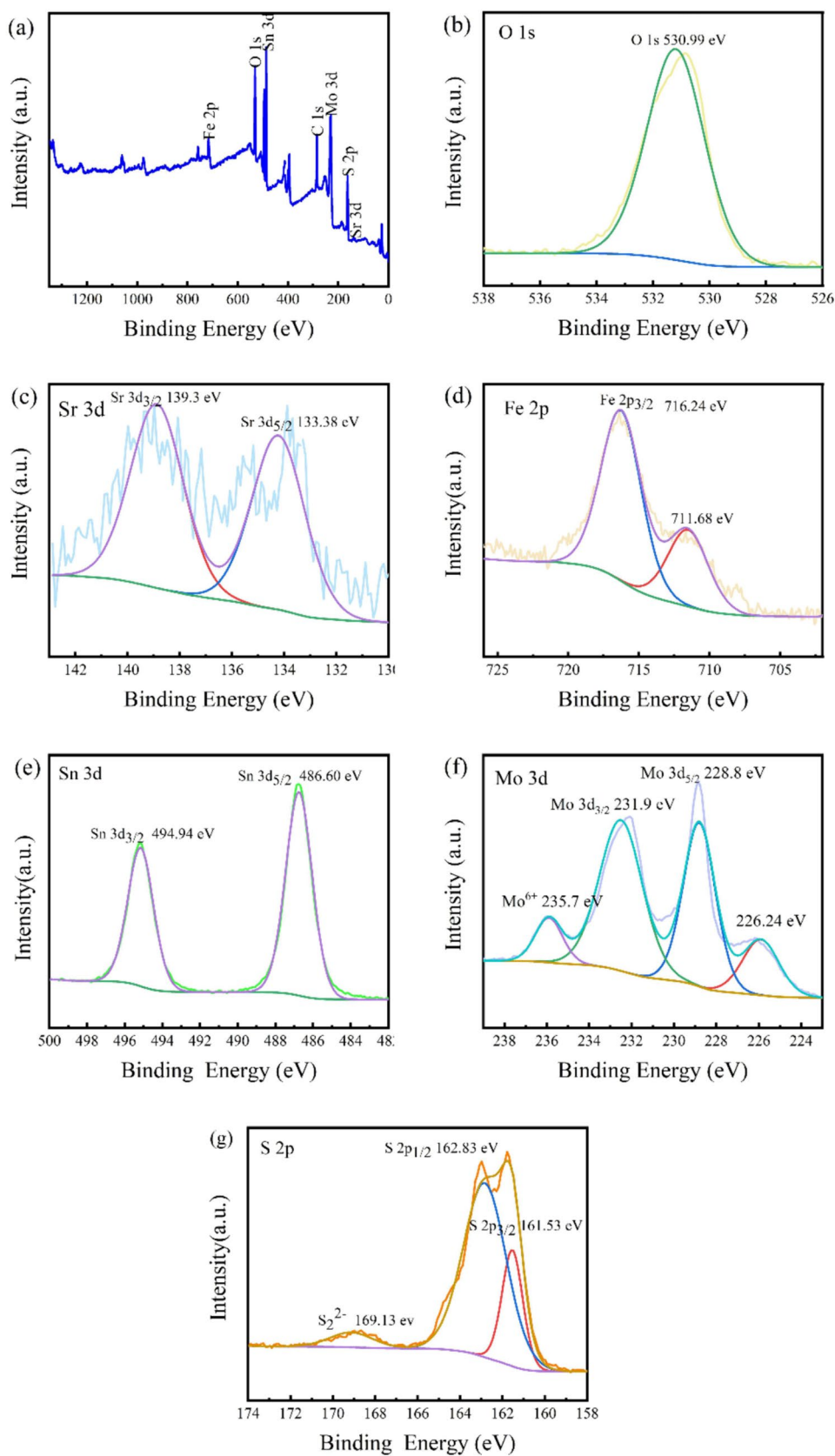
$$(ah\nu)n = -A(h\nu - E_g), \quad (2)$$

where  $h$ ,  $\nu$ ,  $a$ , and  $A$  are Planck's constant, optical frequency, the absorption coefficient, and a constant, respectively [56]. The index  $n$  depends on the electronic transition of the semiconductor, which is directly forbidden. The bandgaps of SnS<sub>2</sub>, SrFe<sub>12</sub>O<sub>19</sub>, SSM-I, SSM-II, SSM-III, and SSM-IV were found to be 2.29, 1.61, 0.72, 1.11, 0.97, and 0.87 eV,

respectively (Fig. 8b, c). Nonetheless, the photocatalytic capacity was boosted by the recombination of SSM-II, which considerably decreased the bandgap and thus substantially prevented the crossover of carriers generated by photons. Information about the division of electron–hole pairs generated by photons can be acquired via PL measurements, which can serve as an indicator of photocatalytic performance. Compared to pristine SrFe<sub>12</sub>O<sub>19</sub>, the photoluminescence intensity of the SSM composites is significantly lower, with SSM-II possessing the lowest photoluminescence intensity among the composite samples (Fig. 8d), which effectively promotes the efficient transfer of electrons at the interface and suppresses the formation of electron–hole pairs, thus extending the lifetime of the photogenerated carriers.

The charge-transfer behavior is investigated using EIS, and the corresponding Nyquist plots are displayed in Fig. 8e. The high-frequency range of the Nyquist graphs for SrFe<sub>12</sub>O<sub>19</sub>, SnS<sub>2</sub>, MoS<sub>2</sub>, and SSM depicts comparable semicircles, the diameters of which increase in the following order: SSM (SSM-I, SSM-II, SSM-III, and

**Fig. 6** XPS profile of the SrFe<sub>12</sub>O<sub>19</sub>/SnS<sub>2</sub>/MoS<sub>2</sub> sample (a); XPS profiles of O 1s (b), Sr 3d (c), Fe 2p (d), Sn 3d (e), Mo 3d (f) and S 2p (g)





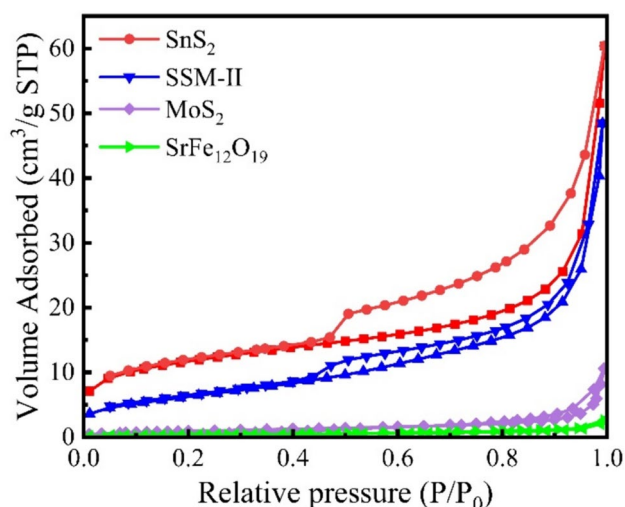


**Fig. 7** N<sub>2</sub> adsorption–desorption isotherms of SnS<sub>2</sub>, MoS<sub>2</sub>, SrFe<sub>12</sub>O<sub>19</sub>, and SSM-II

**Table 1** Specific surface areas and pore structure parameters of the SnS<sub>2</sub>, MoS<sub>2</sub>, SrFe<sub>12</sub>O<sub>19</sub>, and SSM-II materials

Sample	S <sub>BET</sub> (m <sup>2</sup> /g)	Average pore size (nm)	Pore volume (cm <sup>3</sup> /g)
SnS <sub>2</sub>	40.9637	7.6453	0.0479
SrFe <sub>12</sub> O <sub>19</sub>	1.3248	11.2413	0.0020
MoS <sub>2</sub>	3.5768	19.1847	0.0163
SSM-II	22.9599	11.4986	0.0400

SSM-IV) < SnS<sub>2</sub> < MoS<sub>2</sub> < SrFe<sub>12</sub>O<sub>19</sub>. The greatest conductivity and minimum charge-transfer resistance are indicated by SSM-II, which enhances the charge-transfer efficiency between the interfaces. The diameters of SSM-I, SSM-III, and SSM-IV are nearly identical, indicating that the photocatalytic performance of the materials is influenced by their SrFe<sub>12</sub>O<sub>19</sub> content. Among them, SSM-II is more advantageous for the generation and movement of electrons and holes than the other samples [57].

### Photocatalytic Activity

The disintegration of MB during exposure to visible light has been utilized to evaluate the photocatalytic capacity of the photocatalysts. The absorbing spectrum of the SSM-II catalytic material for the MB dye under visible light illumination are displayed in Fig. 9a. The absorption spike characteristic of MB is observed at 664 nm, and MB is uniformly absorbed over the full range of wavelengths. After 30 min of treatment in the dark to establish adsorption–desorption equilibrium, the degradation efficiencies

of the pure SrFe<sub>12</sub>O<sub>19</sub>, SnS<sub>2</sub>, and MoS<sub>2</sub> materials reach 2.50%, 30.00%, and 41.26%, respectively, after 120 min of light exposure. The SSM composite photocatalyst demonstrates increased photocatalytic activity, with SSM-II exhibiting the maximum photocatalytic activity (98.69%) after 120 min of light exposure. Additionally, the first-order kinetic diagram of the decomposition of MB by the synthesized photocatalysts were adapted (Fig. 9c), and the decomposition rate constant (*k*) values were calculated (Table 2) utilizing to the Langmuir–Hinshelwood kinetic model (3) [42]:

$$\ln(C_0/C_t) = kt. \quad (3)$$

The rate constants of SSM-II are approximately 123, 14.47, and 20.5 times higher than those of pure SrFe<sub>12</sub>O<sub>19</sub> (0.0002 min<sup>-1</sup>), SnS<sub>2</sub> (0.0017 min<sup>-1</sup>), and MoS<sub>2</sub> (0.0012 min<sup>-1</sup>), respectively; other SSM composites also show higher rate constants than monophasic materials, which can be improved by incorporating SrFe<sub>12</sub>O<sub>19</sub>. However, the photocatalytic activity of the SSM material decreases as the SrFe<sub>12</sub>O<sub>19</sub> content increases. Excess SrFe<sub>12</sub>O<sub>19</sub> prevents the exposure of SnS<sub>2</sub> active sites, resulting in a smaller effective interfacial contact area. Owing to constant agitation of the aqueous solution and ultraviolet reflection from various particle regions, a limited quantity of photons penetrated the interior heterojunction surface via gaps among the material petals. Thereby producing photogenerated carriers at the heterojunction and extending their lifespan. Moreover, the SrFe<sub>12</sub>O<sub>19</sub> nanosheets uniformly penetrated the SnS<sub>2</sub> nanoflowers, and the SnS<sub>2</sub> nanosheets interacted with microscopic particles of MoS<sub>2</sub> to catalyze transport of electrons and increase the specific surface area of the catalyst. To sum up, the incorporation of SrFe<sub>12</sub>O<sub>19</sub> provides molecules of dye extra spots for adsorption and enables the SSM composite photocatalyst to rapidly degrade the target pollutants.

### Impact of Initial pH

The pH of the solution is a critical and influential operational factor for the degradation of dyes, as it impacts the speed at which dye molecules are adsorbed and desorbed on the exterior of the catalyst, alters the potential of the valence band, and affects the physicochemical characteristics [57, 58]. The impact of pH on the extent of dye degradation by the SSM-II composite is demonstrated in Fig. 10. The pH was adjusted by the addition of dilute aqueous solutions of NaOH (1 M) and HCl (1 M). A weakly acidic environment is the most suitable for the degradation of MB by the SSM composites. The surface charge of the catalyst also depends on the pH

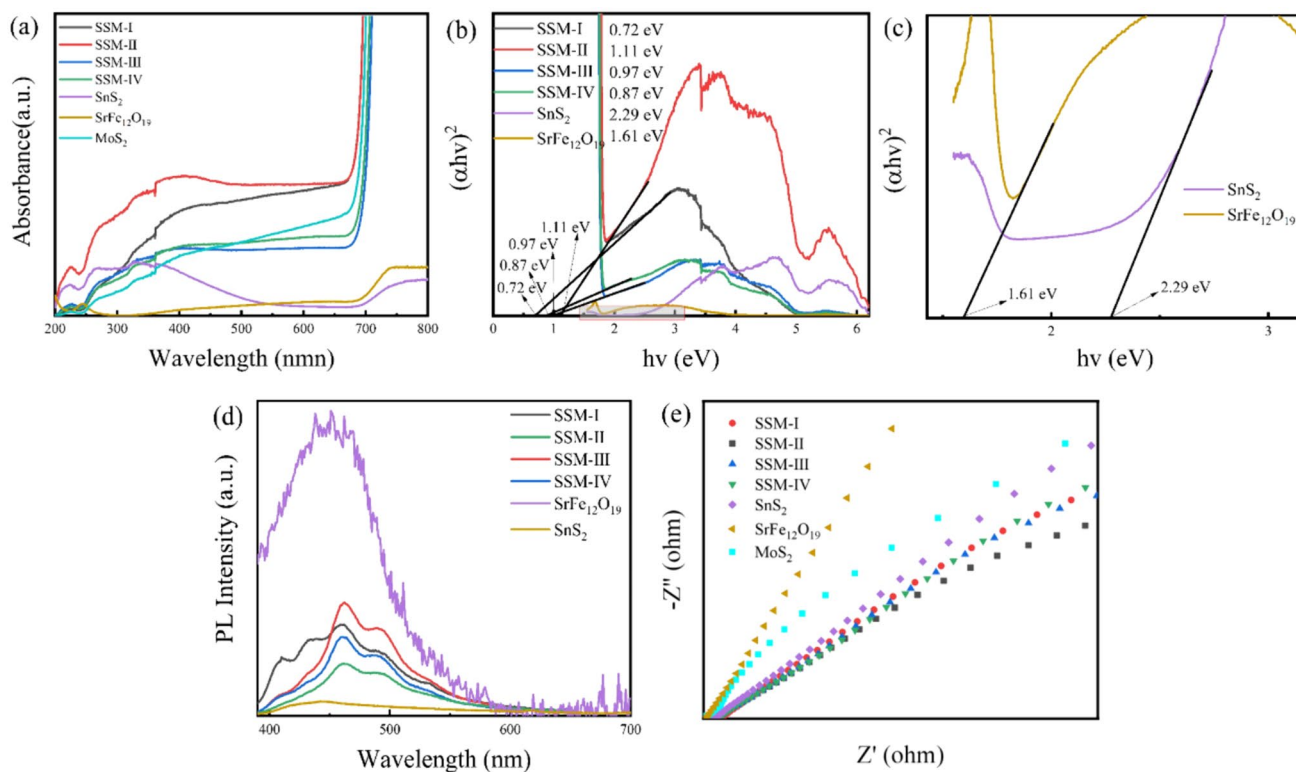


**Fig. 8** UV-Vis DRS profiles of as-prepared MoS<sub>2</sub>, SnS<sub>2</sub>, SrFe<sub>12</sub>O<sub>19</sub>, SSM-I, SSM-II, SSM-III, and SSM-IV (a); corresponding Tauc plots  $(\alpha h\nu)^2$  as a function of  $h\nu$  of SnS<sub>2</sub>, SrFe<sub>12</sub>O<sub>19</sub>, SSM-I, SSM-II, SSM-III, and SSM-IV (b); magnified area showing the E<sub>g</sub> values of SnS<sub>2</sub>

and SrFe<sub>12</sub>O<sub>19</sub> (c); PL spectra of pure SnS<sub>2</sub>, SrFe<sub>12</sub>O<sub>19</sub>, and SSM composites (d); EIS images of as-prepared SnS<sub>2</sub>, MoS<sub>2</sub>, SrFe<sub>12</sub>O<sub>19</sub>, SSM-I, SSM-II, SSM-III, and SSM-IV (e)

of the solution. The quantity of the ionic dye adsorbed by the material is significantly different at pH 6 owing to the electrostatic repulsion between the positive charge on the catalyst surface in the ionic dye and acidic solution. Under alkaline conditions, the produced OH<sup>-</sup> ions combine with H<sup>+</sup> ions on the photocatalyst surface, thereby reducing the adsorption efficiency [59]. The lessened oxidative potential of •OH at higher pH levels (2.8 V at pH 0 as opposed to 1.9 V at pH 7) could be further linked to the decrease in the rate of MB deterioration at higher pH levels.

### Analysis of Active Species Capture Experiments

To identify the SSM-II composite catalyst's photocatalytic response process, research employing free radical capture have been utilized to examine the active species in the photocatalytic process. During 120 min of degradation with the addition of various scavengers, the photocatalytic decomposition rate for 80 mL of the MB (20 mg/L) is demonstrated in Fig. 11. BQ was used as a capturing agent for •O<sub>2</sub><sup>-</sup>, whereas IPA and EDTA-2Na were employed as scavengers of •OH and h<sup>+</sup>, respectively. The decomposition ratio reaches 98.69% during 120 min of light in the

absence of a trapping agent. The addition of EDTA-2Na and IPA reduces the degradation rates to 92.56% and 92.00%, respectively, includes little impact on the efficiency of photocatalysis, demonstrating that the majority of effective catalytic species are neither h<sup>+</sup> and •OH. The photocatalytic degradation rate in the presence of BQ is only 85.13%, suggesting that •O<sub>2</sub><sup>-</sup> is the primary active species in the overall photocatalytic process.

### Photocatalyst Reusability

Figure 12 demonstrates the reusability and stability of the SSM-II photocatalyst. SSM-II maintains a degradation efficiency of 84.07% over three cycles (Fig. 12a b). The crystal structure of the SSM-II material was evaluated using XRD after three cycles of MB degradation under half sunlight intensity (Fig. 12c). The crystal structure is identical both prior to and following photodegradation, based to the patterns of XRD.

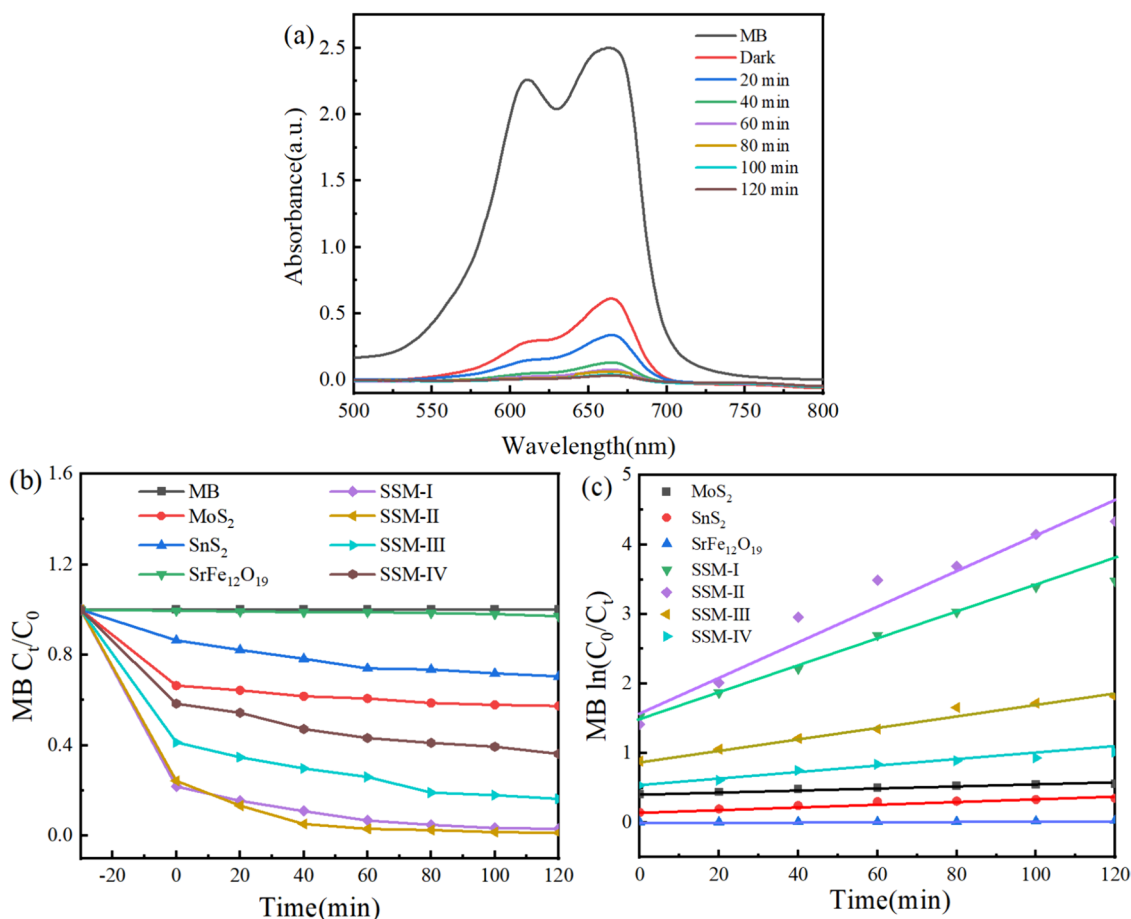


**Fig. 9** Absorption spectra of MB dye degradation by the SSM-II photocatalyst (a); photocatalytic activities of SrFe<sub>12</sub>O<sub>19</sub>, SnS<sub>2</sub>, MoS<sub>2</sub>, SSM-I, SSM-II, SSM-III, and SSM-IV (b); first-order kinetics dia-

gram of the degradation of MB using SrFe<sub>12</sub>O<sub>19</sub>, SnS<sub>2</sub>, MoS<sub>2</sub>, SSM-I, SSM-II, SSM-III, and SSM-IV (c)

## Magnetic Recovery Capability

Figure 13 shows the hysteresis return curves of pure SrFe<sub>12</sub>O<sub>19</sub> and SSM-II. The hysteresis curve of SSM-II exhibits the typical characteristics of hard magnetic materials [60]. The narrow hysteresis return lines indicate that SSM-II has a lower hysteresis loss under alternating

magnetic fields. The saturation magnetization strength ( $M_s$ ) of SSM-II ( $13.78 \text{ emu g}^{-1}$ ) is lower than that of SrFe<sub>12</sub>O<sub>19</sub>; however, both materials can be separated from aqueous solutions equally quickly. The resistance of magnetic materials to demagnetization increases with the coercive force,  $H_{ci}$ . The coercive forces of monophasic SrFe<sub>12</sub>O<sub>19</sub> and SSM-II are 3910.25 and 4161.5 Oe, respectively; thus, SSM-II is slightly more resistant to demagnetization. Photographs of SSM-II and SrFe<sub>12</sub>O<sub>19</sub> exposed to a magnetic field (Fig. 13, inset) illustrate their facile recovery from the dye solution for subsequent recycling.

**Table 2** MB degradation by SrFe<sub>12</sub>O<sub>19</sub>, SnS<sub>2</sub>, MoS<sub>2</sub> and SSM composite photocatalytic materials over time

Photocatalyst	Degradation rate	k (min <sup>-1</sup> )
SSM-I	96.89%	0.0174
SSM-II	98.69%	0.0246
SSM-III	86.61%	0.0081
SSM-IV	63.60%	0.0040
SrFe <sub>12</sub> O <sub>19</sub>	2.50%	0.0002
SnS <sub>2</sub>	30.00%	0.0017
MoS <sub>2</sub>	41.26%	0.0012

## Photocatalytic Mechanism

We indicate a tenable process of degradation of the double heterojunction generated by SSM mixed materials, which accounts for our observations. The enhanced photocatalytic activity of the SSM composites relative to those of pure

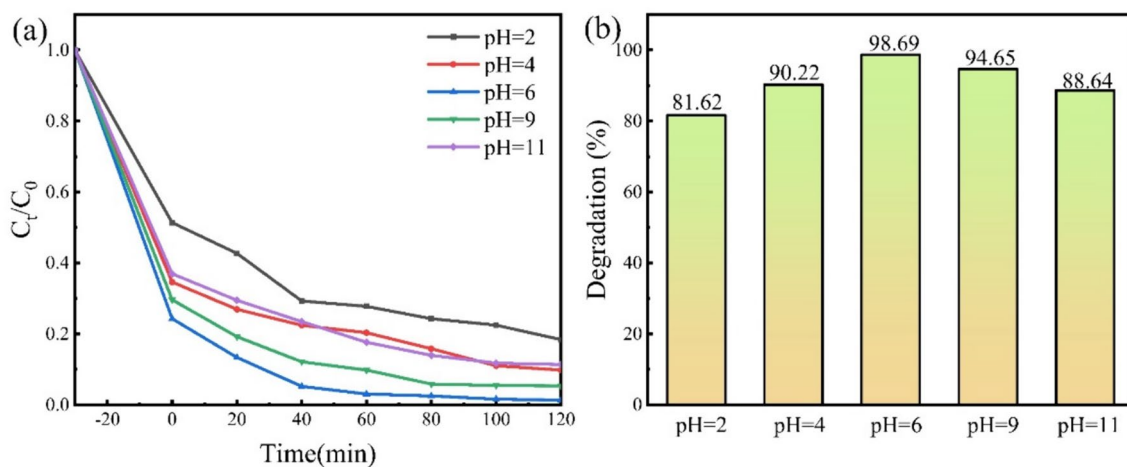


Fig. 10 Degradation of MB by the SSM-II catalyst under different pH conditions

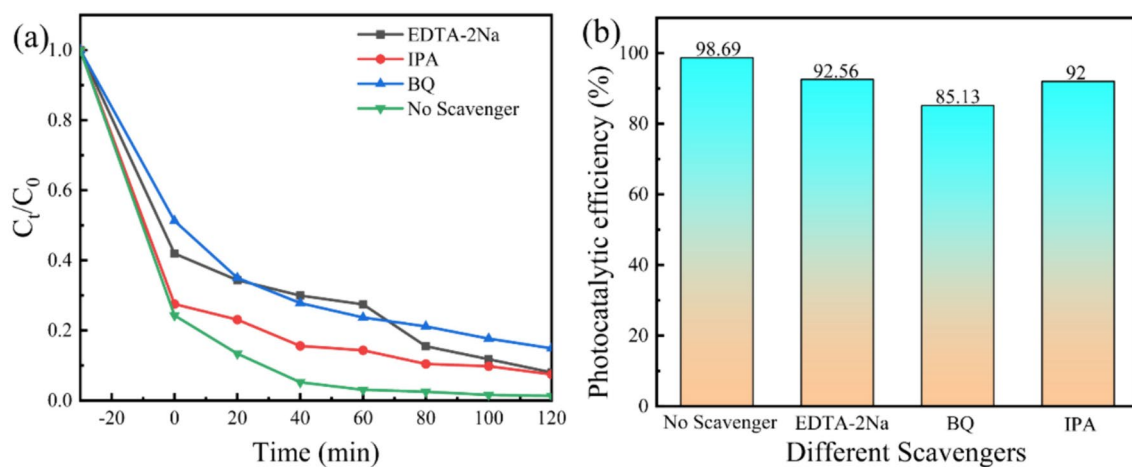


Fig. 11 Impact of active radical scavengers on the photocatalytic activity of SSM-II

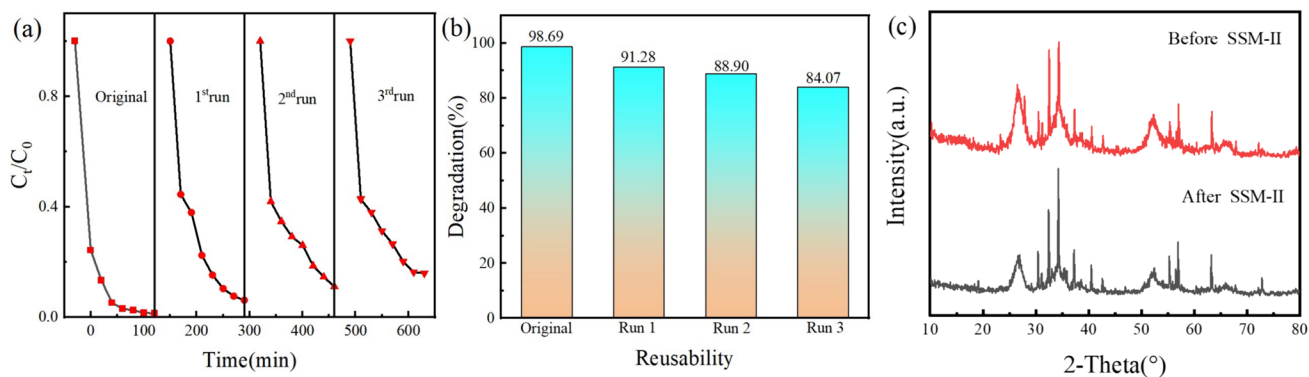
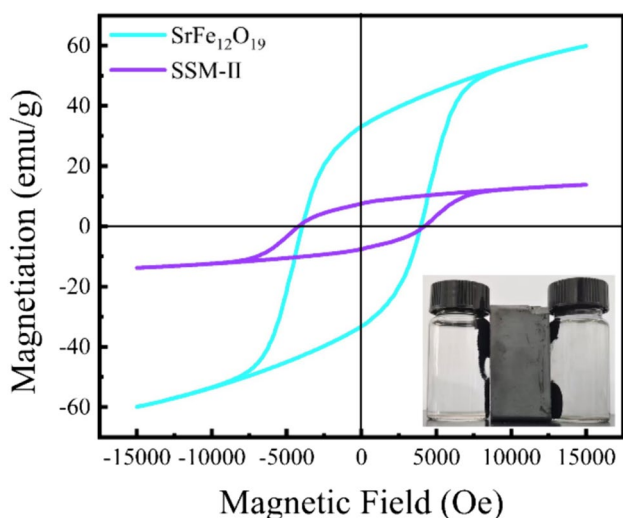
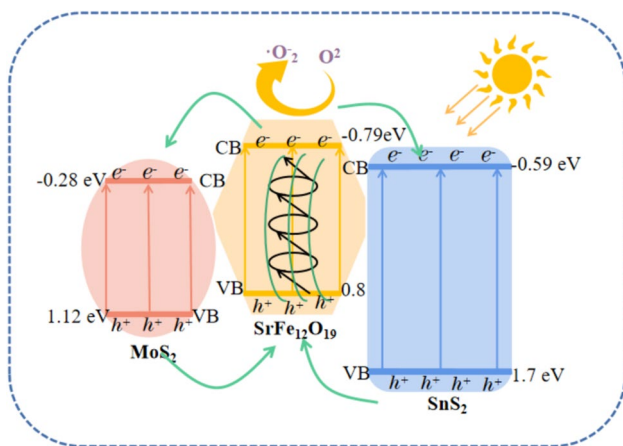


Fig. 12 SSM-II cyclic degradation of MB (a) and degradation performance (b); XRD patterns before and after three cycles (c)



**Fig. 13** Magnetic hysteresis curves of the SrFe<sub>12</sub>O<sub>19</sub> and SSM-II samples



**Fig. 14** Plausible mechanism of charge transfer in SrFe<sub>12</sub>O<sub>19</sub>/SnS<sub>2</sub>/MoS<sub>2</sub> under visible-light irradiation

MoS<sub>2</sub> and SnS<sub>2</sub> was attributed to the formation of type II heterojunctions between the SnS<sub>2</sub>, MoS<sub>2</sub>, and SrFe<sub>12</sub>O<sub>19</sub> semiconductors. Equations (4) and (5) were utilized to calculate the potentials of the valence band ( $E_{VB}$ ) and conduction band ( $E_{CB}$ ), which are shown in Fig. 14.

$$E_{CB} = X - E^e - 0.5E_g, \quad (4)$$

$$E_{VB} = E_{CB} + E_g. \quad (5)$$

Here,  $E^e$  is the potential energy (roughly 4.5 eV for a typical hydrogen electrode),  $X$  is the absolute value of electronegativity, and  $E_g$  is the bandgap [61, 62].

Excitation of the MoS<sub>2</sub> and SnS<sub>2</sub> nanoflowers and hexagonal SrFe<sub>12</sub>O<sub>19</sub> plates under simulated sunlight ( $k > 420$  nm) caused the photoelectrons to migrate from the VB to the CB to initially generate pairings of photoelectron-hole, followed by the formation of electrons and holes on the CB and VB, respectively. Figure 14 shows a possible photocatalytic mechanism. Because the CB of SrFe<sub>12</sub>O<sub>19</sub> ( $-0.79$  eV) is more negative than that of SnS<sub>2</sub> ( $-0.59$  eV) and the VB of SnS<sub>2</sub> ( $1.7$  eV) is more positive than that of SrFe<sub>12</sub>O<sub>19</sub> ( $0.8$  eV), the electrons generated via photosynthesis in the CB of the hexagonal SrFe<sub>12</sub>O<sub>19</sub> plate transition to the CB of the SnS<sub>2</sub> nanoflowers, and the photogenerated holes transition from the MoS<sub>2</sub> nanoflowers to the hexagonal SrFe<sub>12</sub>O<sub>19</sub> plate. Carriers flow across the heterojunction contact, which facilitates photogenerated electron-hole pair separation and hinders recombination. Similarly, MoS<sub>2</sub> and SrFe<sub>12</sub>O<sub>19</sub> also form a type II heterojunction with an internal electric field. Moreover, the magnetic field produced by the magnetic material matrix, in conjunction with the internal electric field, significantly improves the photocatalytic activity. SrFe<sub>12</sub>O<sub>19</sub> creates a stable magnetic field in the ternary composite catalytic material, and some photogenerated electrons move in the direction of the magnetic field. The spiraling motion of the magnetic field and photogenerated carriers accelerate electron migration.

## Conclusions

A magnetically recyclable double-heterojunction nanophotocatalyst, SrFe<sub>12</sub>O<sub>19</sub>/SnS<sub>2</sub>/MoS<sub>2</sub>, was prepared via one-step solvothermal synthesis. The prepared SrFe<sub>12</sub>O<sub>19</sub>/SnS<sub>2</sub>/MoS<sub>2</sub> hybrid photographic catalyst demonstrated both electromagnetic recovery and efficient responsiveness in natural visible-light. The uniformly interspersed SrFe<sub>12</sub>O<sub>19</sub> particles and MoS<sub>2</sub> florets on the SnS<sub>2</sub> nanoflowers effectively modified the crystal structure and morphology of SnS<sub>2</sub>, provided abundant catalytically active sites, and decreased the recombination rate that the electron-hole pairs generated by photons reacted. At pH 6, the SrFe<sub>12</sub>O<sub>19</sub>/SnS<sub>2</sub>/MoS<sub>2</sub> compound obtained an excellent MB decomposition rate of 98.69% under half sunlight intensity. The photocatalytic process ratio of SrFe<sub>12</sub>O<sub>19</sub>/SnS<sub>2</sub>/MoS<sub>2</sub> composites was approximately 123, 14.47, and 20.5 times those of pure SrFe<sub>12</sub>O<sub>19</sub>, SnS<sub>2</sub>, and MoS<sub>2</sub>, respectively. The ratio of photocatalytic decomposition of SrFe<sub>12</sub>O<sub>19</sub>/SnS<sub>2</sub>/MoS<sub>2</sub> remained as high as 84.07% after three cycles, demonstrating its stability. The magnetic response of SrFe<sub>12</sub>O<sub>19</sub>/SnS<sub>2</sub>/MoS<sub>2</sub> facilitates the recycling of contaminated water. Further, owing to its flower-like morphology, it serves as an efficient, environmentally benign photocatalyst for wastewater treatment in a weak sun lighting.

**Acknowledgements** Special thanks to Editage ([www.editage.cn](http://www.editage.cn)) for their English language editing assistance.

**Data availability** The authors declare that the data supporting the findings of this study are available within the paper, its supplementary information files.

## References

1. T. Luukkonen, O. Pehkonen, *Crit. Rev. Environ. Sci. Technol.* **47**, 1 (2016)
2. K. Yin, Y. Xu, X. Li, X. Jin, *J. Clean. Prod.* **197**, 815 (2018)
3. C. Su, Y. Song, M. Umar, *Ocean Coast. Manag. Manag.* **204**, 105550 (2021)
4. J. Luo, R. Li, Y. Chen, X. Zhou, X. Ning, L. Zhan, L. Ma, X. Xu, L. Xu, L. Zhang, *Sep. Purif. Technol. Purif. Technol.* **210**, 417 (2019)
5. A. Fujishima, K. Honda, *Nature* **238**, 37 (1972)
6. R. Lavanya, T. Ramakrishnappa, K. M. Girish, K. Suresh Kumar, M. Radhakrishna Reddy, H. R. Prakash, *Bulletin of Materials Science* **47**, 34 (2024).
7. M.P. Mazhari, H. Khojasteh, N. Sharifi, P. Aspoukeh, S.M. Mousavi, *J. Sol-Gel Sci. Technol.* **110**, 156 (2024)
8. N. Akram, J. Guo, W. Ma, Y. Guo, A. Hassan, J. Wang, *Sci. Rep.* **10**, 1939 (2020)
9. Z. Li, X. Meng, Z. Zhang, *J. Photochem. Photobiol., C* **35**, 39 (2018)
10. Z. Cui, H. Wu, K. Bai, X. Chen, E. Li, Y. Shen, M. Wang, *Physica E E* **144**, 115361 (2022)
11. X. Zhou, J. Zou, S. Zhang, M. Pan, W. Gong, *Chin. J. Catal. Catal.* **38**, 287 (2017)
12. R. Zhang, L. Bi, D. Wang, Y. Lin, X. Zou, T. Xie, Z. Li, *J. Colloid Interface Sci.* **578**, 431 (2020)
13. X. Yang, W. Xin, X. Yin, X. Shao, *Chem. Phys. Lett.* **651**, 127 (2016)
14. L. Ding, Z. Zhang, Z. Wen, F. You, N. Hao, J. Wei, J. Qian, K. Wang, *Sens. Actuators, B Chem.* **367**, 132033 (2022)
15. B. Xue, H. Jiang, T. Sun, F. Mao, J. Wu, *Mater. Lett.* **228**, 475 (2018)
16. X. Yuan, H. Wang, Y. Wu, X. Chen, G. Zeng, L. Leng, C. Zhang, *Catal. Commun. Commun.* **61**, 62 (2015)
17. K. Mohammadi, M. Sadeghi, R. Azimirad, *J. Mater. Sci.* **28**, 10042 (2017)
18. Y. Liu, X. Mi, J. Wang, M. Li, D. Fan, H. Lu, X. Chen, *Inorganic Chemistry Frontiers* **6**, 948 (2019)
19. J. Wang, Y. Chen, *Colloid and Interface Science Communications* **45**, 100522 (2021)
20. L. Dashairya, M. Sharma, S. Basu, P. Saha, *J. Alloy. Compd.* **774**, 625 (2019)
21. A. Zhang, Z. Nan, *J. Therm. Anal. Calorim. Calorim.* **139**, 217 (2019)
22. J. Kang, C. Jin, Z. Li, M. Wang, Z. Chen, Y. Wang, *J. Alloy. Compd.* **825**, 153975 (2020)
23. X. Chen, C. Zhao, H. Wu, Y. Shi, C. Chen, X. Zhou, *Materials* **15**, 3786 (2022)
24. D. Park, M. Kim, J. Kim, *J. Alloy. Compd.* **925**, 166623 (2022)
25. Z. Mei, G. Wang, S. Yan, J. Wang, *Acta Physico Chimica Sinica* **37**, 2009097 (2020)
26. Y. Zeng, N. Guo, Y. Song, Y. Zhao, H. Li, X. Xu, J. Qiu, H. Yu, *J. Colloid Interface Sci.* **514**, 664 (2018)
27. X. Man, L. Yu, J. Sun, S. Li, *Funct. Mater. Lett.. Mater. Lett.* **09**, 1650065 (2016)
28. M. Wu, L. Li, N. Liu, D. Wang, Y. Xue, L. Tang, *Process. Saf. Environ. Prot. Saf. Environ. Prot.* **118**, 40 (2018)
29. K. Zhu, L. Luo, T. Peng, *Journal of Wuhan University of Technology-Mater. Sci. Ed.* **34**, 883 (2019)
30. Y. Wang, Y. Ni, *Anal. Chem.* **86**, 7463 (2014)
31. M. Ghanei-Motlagh, M.A. Taher, *Biosens. Bioelectron.. Bioelectron.* **109**, 279 (2018)
32. X. Lin, F. Wang, X. Shan, Y. Miao, X. Chen, M. Yan, L. Zhang, K. Liu, J. Luo, K. Zhang, *Appl. Surf. Sci.* **546**, 149074 (2021)
33. L. Song, T. Wang, W. Jing, X. Xie, P. Du, J. Xiong, *Mater. Res. Bull.* **118**, 110522 (2019)
34. E.S. Sowbakkivavathi, V. Murugadoss, R. Sittaramane, S. Angaiah, *J. Solid State Electrochem. Electrochem.* **24**, 2289 (2020)
35. J. Ye, C. Cheng, J. Lin, C. Huang, T. Yeh, C. Hsieh, *Surf. Coat. Technol.* **394**, 125855 (2020)
36. C. Sun, K. Zhao, Y. He, J. Zheng, *ACS Appl. Mater. Interfaces* **11**, 20762 (2019)
37. J. Wan, Y. Hao, Y. Shi, Y. Song, H. Yan, J. Zheng, R. Wen, L. Wan, *Nat. Commun. Commun.* **10**, 3265 (2019)
38. H. Kaur, A. Rai, S.S. Bhatia, *Mod. Phys. Lett. A* **34**, 1950313 (2019)
39. N.A. Algarou, Y. Slimani, M.A. Almessiere, F.S. Alahmari, M.G. Vakhitov, D.S. Klygach, S.V. Trukhanov, A.V. Trukhanov, A. Baykal, *J. Market. Res.* **9**, 5858 (2020)
40. P. Maltoni, T. Sarkar, G. Barucca, G. Varvaro, F. Locardi, D. Peddis, R. Mathieu, *The Journal of Physical Chemistry C* **125**, 5927 (2021)
41. Q. Wu, Z. Yu, Y. Wu, Z. Gao, H. Xie, J. Magn. Magn. Mater. Magn. Mater. **465**, 1 (2018)
42. S. Chen, Y. Di, H. Li, M. Wang, B. Jia, R. Xu, X. Liu, *Appl. Surf. Sci.* **559**, 149855 (2021)
43. T. Xie, L. Xu, C. Liu, Y. Wang, *Appl. Surf. Sci.* **273**, 684 (2013)
44. Z. Yang, Y.W. Chen, Y.F. Jin, Z. Jin, H.S. Xie, X.S. Cong, D.G. Teng, *ACS Omega* **9**, 11356 (2024)
45. H. Peng, X. Yang, P. Zhang, Y. Zhang, C. Liu, D. Liu, J. Gui, *RSC Adv.* **7**, 50216 (2017)
46. Y. Liu, P. Feng, Z. Wang, X. Jiao, F. Akhtar, *Sci. Rep.* **7**, 1845 (2017)
47. Y. Li, S. Tan, Y. Meng, Y. Xia, L. Gao, W. Chen, *J. Mater. Sci. Mater. Electron.* **33**, 13887 (2022)
48. N.S. Das, A. Roy, A. Chowdhury, *Lett Appl NanoBioScience* **12**, 47 (2022)
49. N. Anitha, M. Anitha, J. Raj Mohamed, S. Valanarasu, L. Amalraj, *Journal of Materials Science: Materials in Electronics* **29**, 11529 (2018).
50. J. Zhou, Z. Zhang, X. Kong, F. He, R. Zhao, R. Wu, T. Wei, L. Wang, J. Feng, *Appl. Surf. Sci.* **510**, 145442 (2020)
51. J. Wu, R. Zhao, H. Xiang, C. Yang, W. Zhong, C. Zhang, Q. Zhang, X. Li, N. Yang, *Appl. Catal. BCatal. BCatal.* **B 292**, 120200 (2021)
52. D.D. Mishra, G. Tan, *J. Phys. Chem. Solids* **123**, 157 (2018)
53. Y. Zeng, N. Guo, H. Li, Q. Wang, X. Xu, Y. Yu, X. Han, H. Yu, *Sci. Total. Environ.* **659**, 20 (2019)
54. X. Hu, G. Wang, J. Wang, Z. Hu, Y. Su, *Appl. Surf. Sci.* **511**, 145499 (2020)
55. Y. Liu, X. Xu, J. Zhang, H. Zhang, W. Tian, X. Li, M.O. Tade, H. Sun, S. Wang, *Appl. Catal. BCatal. BCatal.* **B 239**, 334 (2018)
56. X. Yuan, X. Xue, H. Ma, S. Guo, L. Cheng, *Nanotechnology* **28**, 375705 (2017)
57. S. Xing, Z. Zhou, Z. Ma, Y. Wu, *Appl. Catal. BCatal. BCatal.* **B 107**, 386 (2011)
58. M. Abbas, B.P. Rao, V. Reddy, C. Kim, *Ceram. Int.* **40**, 11177 (2014)
59. S. Miao, Z. Zha, Y. Li, X. Geng, J. Yang, S. Cui, J. Yang, *J. Photochem. Photobiol., A* **380**, 111862 (2019)

60. A.H. Mady, M.L. Baynosa, D. Tuma, J.J. Shim, Appl. Catal. BCatal. B **203**, 416 (2017)
61. M. Sattari, M. Farhadian, A. Reza Solaimany Nazar, M. Moghadam, *Journal of Photochemistry and Photobiology A: Chemistry* **431**, 114065 (2022).
62. B. Akhsassi, Y. Ettahiri, B. Bakiz, A. Taoufyq, S. Villain, C. Favotto, F. Guinneton, J.R. Gavarri, A. Benlhachemi, Colloids Surf. A **673**, 131762 (2023)

Springer Nature or its licensor (e.g. a society or other partner) holds exclusive rights to this article under a publishing agreement with the author(s) or other rightsholder(s); author self-archiving of the accepted manuscript version of this article is solely governed by the terms of such publishing agreement and applicable law.

**Publisher's Note** Springer Nature remains neutral with regard to jurisdictional claims in published maps and institutional affiliations.